Extending SMO into the lens pupil domain

Monica Kempsell Sears*, Germain Fenger, Julien Mailfert, Bruce Smith
Rochester Institute of Technology, Microsystems Engineering, 77 Lomb Memorial Drive,
Rochester, NY 14623

ABSTRACT

As semiconductor lithography is pushed to smaller dimensions, the process yields tend to suffer due to sub-wavelength imaging effects. In response, resolution enhancement technologies have been employed together with optimization techniques, specifically source mask optimization (SMO), which finely tunes the process by simultaneously optimizing the source shape and mask features. However, SMO has a limitation in that it fails to compensate for undesired phase effects. For mask features on the order of the wavelength, the topography of the mask can induce aberrations which bring asymmetry to the focus-exposure matrix (FEM) and ultimately decrease the process window. This paper examines the dependency of FEM asymmetry on factors such as the illumination coherency and lens induced spherical aberration. It is shown that lens induced primary spherical aberration strongly impacts the symmetry of the FEM. In this work, phase correction is achieved by incorporating the pupil plane in an optimization. It is shown that primary spherical aberration can correct for effects including the degraded depth of focus and the tilt in the FEM for a dual trench mask. A pupil function with an optimized coefficient of primary spherical aberration balances the spherical aberration induced by the mask topography.
Keywords: Source Mask Optimization (SMO), Focus Exposure Matrix (FEM) tilt, mask topography, phase pupil filter, spherical aberration

1. INTRODUCTION

Source mask optimization (SMO) represents the simultaneous adjustment of lithographic mask and source parameters in order to optimize the image quality. Gau *et al.* proposed the Archel method, which divides the source into regions with the same collected diffraction orders, and then selects the source regions based on an imaging quality metric, such as depth of focus (DOF) [1]. Rosenbluth *et al.* used a Fourier Transform method to calculate the mask pattern that provides the optimized wave front, thus performing joint source and mask optimization. This method was able to greatly enhance the process window [2]. However, source optimization is limited to controlling the magnitude and placement of diffraction energy in the lens pupil, and phase control is limited to that made available through phase shifting at the mask plane. As mask features are becoming sub-wavelength, additional degrees of freedom are needed for engineering diffraction energy in terms of location, amplitude, and phase in order to accommodate mask topography effects [3, 4].

In this paper, some fundamental issues involving the interaction of source and mask parameters are addressed to understand the importance of phase control in the objective lens pupil domain. The task is a rather large one, made so by the large number of source and mask combinations for specific device geometries, together with the computational expense that would be required to co-optimize three rather than two domains. The task, therefore, is broken down into stages where the first stage will be presented here. Consideration will be made of various mask types (AltPSM, AttPSM, and binary), source types (small σ conventional, parametric, freeform) and the influence that the lens pupil may offer. Although amplitude filtering in the lens pupil does allow for wavefront engineering, the phase content is of most importance [5-7]. Description of pupil filtering functions will be carried out through conventional wavefront description, specifically through Zernike polynomials. The goal then becomes the identification of combinations of source, mask, and pupil functions that lead to the most robust imaging process.

The case that will be presented here is one involving a strong alternating phase shift mask (AltPSM) imaged with small partial coherence. Specifically, a dual-trench mask is chosen together with a partial coherence factor of 0.3 so that three dimensional mask topography effects can be balanced [8]. It is known that such an imaging scenario will lead to asymmetric imaging for sub-wavelength imaging. This manifests in phenomena such as the best focus shift through pitch and a tilt in the focus-exposure matrix [9]. To address this effect, the asymmetry of the focus exposure matrix (FEM) is evaluated with respect to the source coherency and lens induced spherical aberration. The effect of mask topography on FEM symmetry is also evaluated. This is followed by an optimization procedure for improving FEM symmetry and/or DOF.

2. FEM TILT STUDY

Spherical aberration was evaluated in this study due to the angular dependence of the focal point imaged through a plane parallel plate, governed by Snell's Law [10]. Accordingly, spherical aberration is expected to be induced by the mask, although the situation is made more complicated by topographical features and deep etch depths.

Unexpected phase differences between the diffraction orders can cause undesired phenomena, such as the asymmetry in the FEM, deemed FEM Tilt. In this study, the aerial image (AI) FEM was evaluated in order to exclude photoresist effects. The following simulation study was conducted in order to gain an understanding of its dependency on source coherency and spherical aberration present in the lens system. KLA-Tencor PROLITH™ was used, with the rigorous Maxwell model unless otherwise noted. The study was performed on a binary test case with 1200 nm pitch and 600 nm line, with a wavelength of 365 nm, a partial coherence (σ) of 0.3, and a numerical aperture (NA) of 0.5. A large pitch was used in order to first evaluate the impact of spherical aberration in the lens without mask topography effects. In order to evaluate the effects of mask topography, a chromium oxide on quartz dual trench ($\pi/3\pi$) AltPSM with 90 nm pitch and 45 nm line was used with a system of 193 nm wavelength, σ of 0.3, and NA of 1.35. Depth of focus was calculated by measuring the line CDs with a ±10% CD specification at a 3% exposure latitude around the best exposure.

Fringe Zernike normalization is used to describe 3rd order (primary) spherical aberration, where z_9 represents the primary spherical coefficient [11]. The phase as a function of pupil radius becomes

$$\Phi(\rho) = z_9\,(6\rho^4 - 6\rho^2+1) \qquad (1)$$

This representation is normalized to the maximum, so that the polynomial has a maximum value of unity when z_9 is 1. With this coefficient, the phase is 2π radians at the edge of the pupil, or 1 full wavelength of wavefront deformation. In the following exercises, the effect of spherical aberration is observed by varying the coefficient z_9.

2.1 Lens induced spherical aberration

A wavefront with spherical aberration causes the best focus (BF) to shift [10]. The lens induced spherical aberration causes a BF shift in the aerial image FEM according to the sign of the coefficient, shown in Figure 1. With a large positive lens induced 3rd order spherical aberration of +0.3, the FEM has a negative FEM Tilt, and with a large negative z_9 of -0.3, the FEM has a positive FEM Tilt.

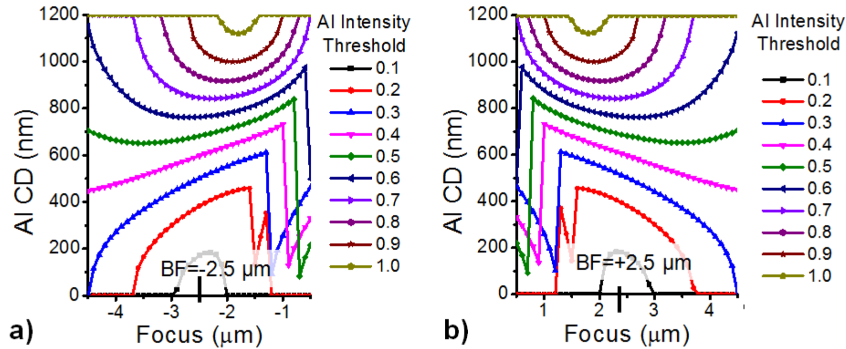

Figure 1. Aerial image FEM due to (a) large negative z_9 of -0.3 has a negative BF shift and a positive FEM Tilt and (b) large positive z_9 of +0.3 has a positive BF shift and a negative FEM Tilt

The corresponding aerial image through focus with the large positive spherical aberration of Figure 1b is shown in Figure 2. The lens induced primary spherical aberration causes the aerial image to no longer contain an isofocal point, meaning there is no exposure that will allow the CD to be constant through focus. Instead, the CD changes linearly with focus, giving the tilted appearance to the FEM. The best focus was shifted from 0 µm to +2.5 µm, showing spherical aberration's tendency to shift the best focus.

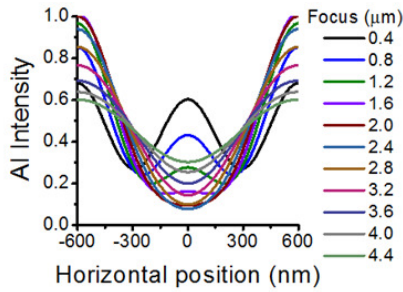

Figure 2. With lens induced spherical aberration z_9 of +0.3, the aerial image through focus with partially coherent σ of 0.3 has no isofocal point

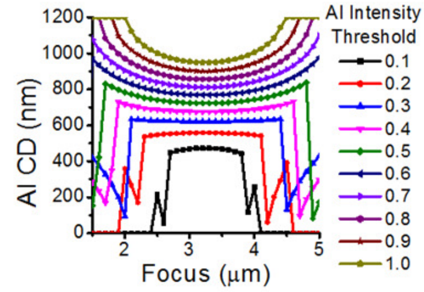

Figure 3. Even with lens induced spherical aberration z_9 of +0.3, the aerial image FEM with coherent illumination (σ of 0) has improved symmetry over Figure 1b

2.2 Coherency

The aerial image FEM Tilt is strongly dependent on the coherency of the source. Figure 1b shows the simulation of a binary mask with pitch of 1200 nm, *σ* of 0.3, wavelength of 365 nm, and NA of 0.5, revealing asymmetry due to the lens induced primary spherical aberration of +0.3. However, if a coherent source is used, then the FEM Tilt is reduced, shown in Figure 3 as a symmetric FEM. An explanation for this effect will be discussed in section 2.4.

For a coherent source, an isofocal point appears in the aerial image and thus a symmetric FEM is observed even with a z_9 of +0.3, seen in Figure 4a. The lens spherical aberration does induce a BF shift of +3.25 µm, as expected. The isofocal point is removed by using a small σ dipole source with center sigma (σ_C) of 0.1 and radius sigma (σ_R) of 0, shown in Figure 4b. The aerial image from this small σ dipole source represents the imaging provided by the edge source point at a σ of 0.1, thus sampling a partially coherent source. This simulation shows that the imaging from this off axis source point does not allow an isofocal point, even though it is essentially a coherent source. This reveals that FEM Tilt does not require the numerous directions of plane waves from a partially coherent source. In the presence of spherical aberration, FEM Tilt can be triggered by an off-axis point source mirrored for source symmetry.

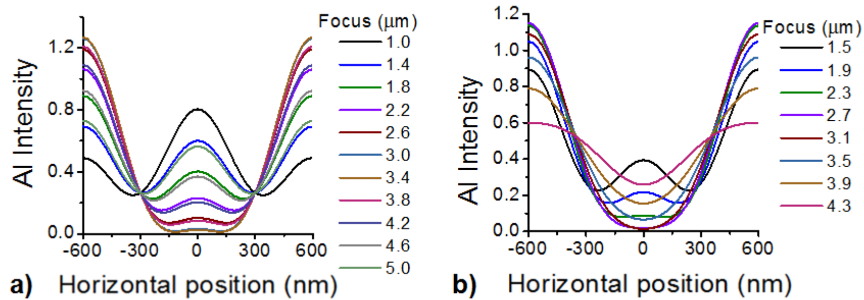

Figure 4. Aerial image through focus with z_9 of +0.3 and (a) a coherent source has an isofocal point and (b) σ_C of 0.1 σ_R of 0 dipole source has no isofocal point

2.3 Mask topography

When feature sizes on the mask are on the order of the wavelength, the mask topography can induce aberrations which induce asymmetry in the FEM [9]. For the dual trench AltPSM 90 nm pitch test case, the FEM Tilt was observed to be symmetric through z_9 about a z_9 of 0 (See Section 4.2 for more details). Figure 5 shows the effect that z_9 has on the BF shift; a negative z_9 induces a positive BF shift, and a positive z_9 induces a negative BF shift. Note that at a z_9 of both -0.15 and +0.15, the FEM Tilt is positive.

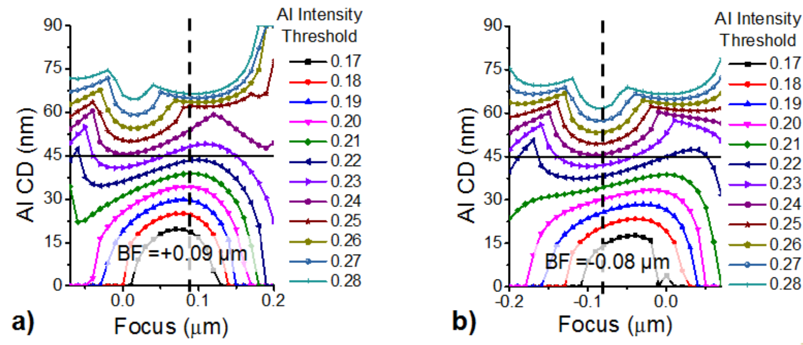

Figure 5. AltPSM aerial image FEM with (a) z_9 of -0.15 has positive BF shift and (b) z_9 of +0.15 has negative BF shift

Figure 6 shows the aerial image FEM and aerial image through focus for both a coherent source and a partially coherent source with σ of 0.3. With the partially coherent source, the FEM contains a negative FEM Tilt, and the aerial image through focus does not contain an isofocal point. With coherent illumination, the FEM is symmetric and the aerial image through focus does contain an isofocal point. This relationship to coherency is characteristic of spherical aberration, as discussed in the previous section. With both sources, the best focus is shifted slightly positive, characteristic of negative primary spherical aberration, as seen in Figure 5. This suggests that a lens induced positive spherical aberration may compensate for the aberrations induced by the mask topography.

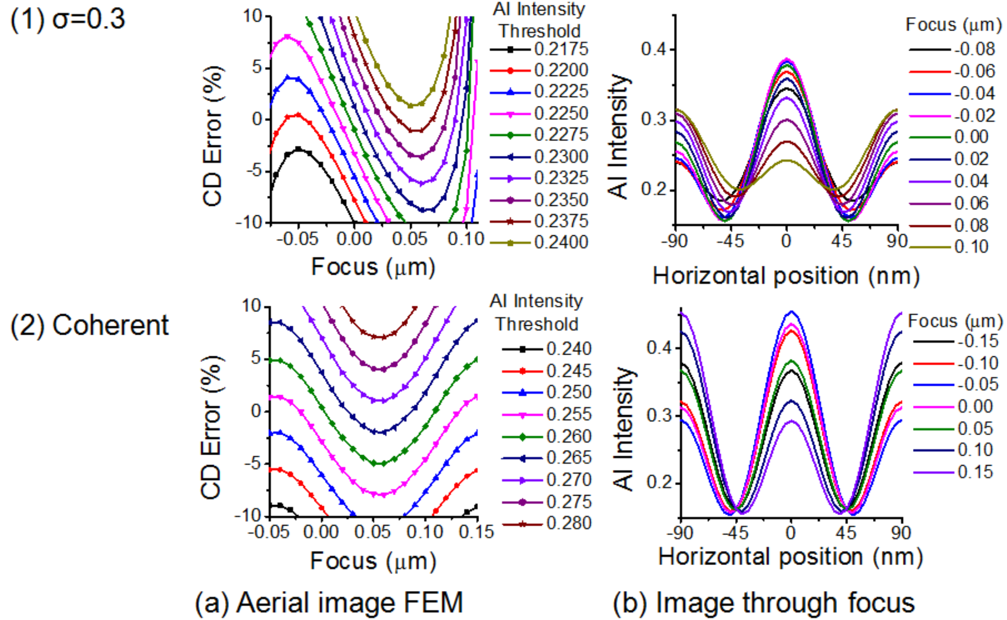

Figure 6. AltPSM aerial image (a) FEM and (b) through focus for (1) a σ of 0.3 source shows FEM asymmetry and no isofocal point and (2) coherent source shows FEM symmetry and isofocal point

2.4 Explanation of OAI effect

The reason why coherent illumination allows a more symmetric FEM can be explained with the simple diagram in Figure 7. A lens induced primary spherical aberration is shown, following the Fringe Zernike normalization [11]. The locations of example 0th and $\pm 1^{st}$ diffraction orders are shown for both an on-axis and an off-axis source point. Even with a large spherical aberration coefficient, the induced phases from the diffraction orders from an on-axis source point can lie on a quadratic function, which models first order defocus, shown in Figure 7a. Thus, even though there is spherical aberration, it can be modeled and perceived as defocus. However, for an off-axis source point, the shifted diffraction orders no longer have phase values that can all be approximated by an axially symmetric quadratic function. Thus, the effect on the image is not as simple as a shift in focus. The isofocal point disappears and the CD becomes linearly related to focus, resulting in a tilted FEM.

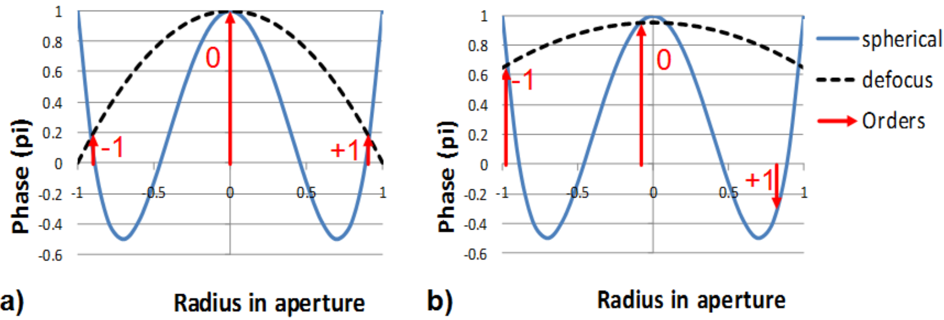

Figure 7. Primary spherical aberration is shown in solid and the diffraction orders are shown as arrows. The induced phases for (a) an on-axis point source can be modeled as defocus, shown as dashed, (b) but for an off-axis point source cannot

3. OPTIMIZATION APPROACH

The lithographic system was simulated with a commercial lithography simulator, KLA-Tencor PROLITH^{TM}, which uses vector diffraction modeling so it can include effects such as polarization and mask topography. The simulator can also include aberrations and pupil filters. These simulations were integrated with Matlab, a numerical computing environment and programming language, in order to utilize data manipulation capabilities and automatic optimization. The integration was completed using the PROLITH^{TM} Programming Interface, or PPI. Matlab was used to set up the simulation in PROLITH and then directly output the DOF and calculate the symmetry of the FEM.

Aerial images were calculated in order to evaluate the impact of the mask topography without the effect of photoresist. 1D mask layouts were used in order to conform to the gridded design layouts currently used by industry [12]. The mask was an unbiased dual trench (π/3π) alternating phase shift mask (AltPSM) of chromium oxide on quartz, with etch depths of 85.7/257.1 nm, duty ratio of 1:1, and a pitch of 90, 100, or 110 nm. The source shape was un-polarized partially coherent with σ of 0.3, a 193 nm wavelength, and NA of 1.35.

The coefficient of 3rd order spherical aberration was optimized in order to maximize FEM symmetry or process window. Since there was only one variable, a simple exhaustive grid search over the z_9 parameter space was performed. The metric used to quantify the symmetry of the aerial image FEM was termed FEM Tilt. FEM Tilt was calculated by extracting the linear coefficient (b) from a polynomial in focus ($a\mathrm{F}^2+b\mathrm{F}+c$) fitted to the FEM within the process window. An FEM Tilt of zero would represent a symmetric FEM, such as that calculated with the Kirchhoff approximation, shown in Figure 8a, thus a smaller FEM Tilt was more desirable.

4. OPTIMIZATION RESULTS

4.1 3D mask topography effects

When the mask features are on the order of the wavelength, the 3D topography of the mask induces aberrations which enhance the asymmetry of the FEM. An aerial image simulation performed with the Kirchhoff approximation is shown in Figure 8a, which shows symmetry about a best focus of 0 µm. Using a ±10% CD specification around the 45 nm target and a 3% exposure latitude requirement, the DOF is 200 nm. However, for the same input parameters except using the rigorous Maxwell model to represent the 3D topography of the mask, the FEM is degraded, shown in Figure 8b. The 3D mask effects reduce the DOF to only 120 nm. It would be desirable to use a pupil filter to compensate for the aberrations induced by the mask in order to achieve a more symmetric FEM, thus a higher process window. If an optimized pupil filter provided an FEM identical to that of the Kirchhoff approximation, then it would represent the inverse of the aberrations induced by the mask.

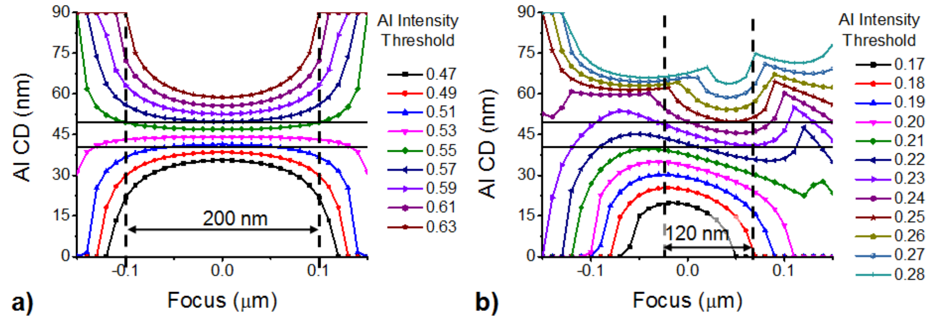

Figure 8. Aerial image FEM for an AltPSM with 90 nm pitch and σ of 0.3 with (a) Kirchhoff approximation has a DOF of 200 nm and an FEM Tilt of 0.00 and (b) rigorous Maxwell model has a DOF of 120 nm and an FEM Tilt of -0.54

4.2 Optimization of primary spherical aberration

The 90 nm pitch AltPSM test case was used, as discussed previously. The aerial image with no induced spherical aberration is degraded due to the 3D mask topography, seen in Figure 6. The resulting FEM Tilt and DOF values from an exhaustive search of z_9 are shown in Figure 9. The exhaustive search was performed at three different pitches to determine if a spherical aberration could be beneficial to all of them.

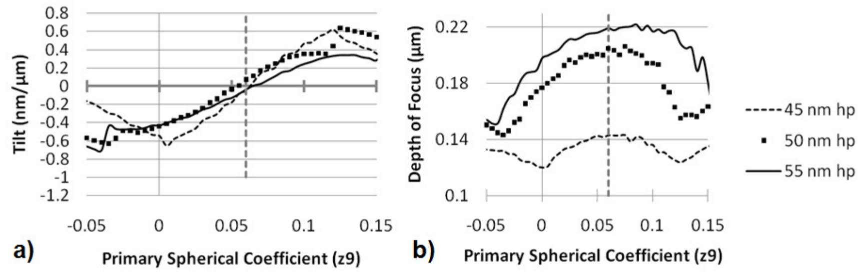

Figure 9. Exhaustive z_9 grid search of (a) FEM Tilt and (b) DOF for 45, 50, and 55 nm half pitch. z_9 of +0.06 is dashed

The FEM Tilt is near zero at z_9 of +0.06 for all three pitches, which shows that the FEM from all three pitches is symmetric at this point. The FEM Tilt has been reduced by at least 10 times over the FEM Tilt which occurs at z_9 of 0. At this z_9 of +0.06, the 45 nm hp DOF of 142 nm is improved by 19% over the DOF at z_9 of 0. The 50 nm hp and 55 nm hp received DOF improvements of 16% and 11%, respectively. The optimized value of z_9 is positive, which is consistent for mask topography inducing a negative value of primary spherical aberration.

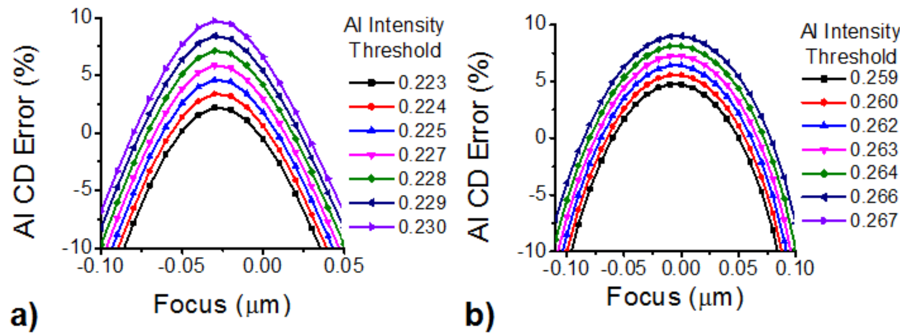

Figure 10. Aerial image FEM with z_9 of +0.06 for (a) 45 nm hp and (b) 50 nm hp

The resulting FEMs at the optimized z_9 of +0.06 for 45 and 50 nm hp are shown in Figure 10. Not only is there a 19% improvement in DOF for the 45 nm hp, but the FEM Tilt has been reduced from -0.54 to -0.05, providing a more symmetric FEM. The FEM Tilt has been reduced from 0.44 to 0.01 for the 55 nm hp.

4.3 Optimized pupil filter

The shape of the optimized pupil filter which gives the smallest FEM Tilt is shown in Figure 11. The location of the diffraction orders for 45 nm hp mask with a σ of 0.3 source are given for reference. Since an FEM under the Kirchhoff approximation with no aberrations is perfectly symmetric, this pupil filter provides the closest compensation to balance the aberrations from mask topography. Thus, the aberrations induced by the mask topography can be estimated to be the inverse of the optimized value, or a z_9 of -0.06.

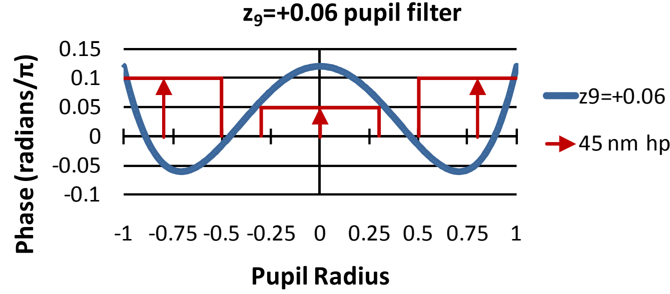

Figure 11. Shape of optimized pupil filter that results in the smallest FEM Tilt. The locations of the diffraction orders for 45 nm hp are shown for reference with a σ of 0.3 source.

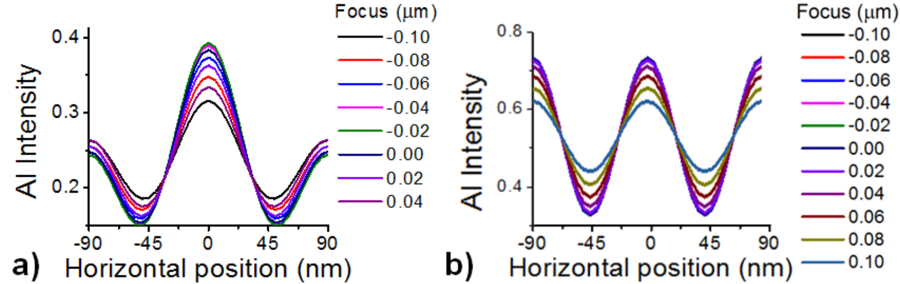

Figure 12. Aerial image through focus for 45 nm hp with (a) rigorous Maxwell (with z_9 of +0.06) and (b) Kirchhoff approximation

However, the pupil filter does not provide perfect compensation, since the aerial image through focus is not identical to an aerial image under the Kirchhoff approximation, as shown in Figure 12. The Maxwell aerial image through focus contains one cross over point, whereas the Kirchhoff contains two. An optimization including other higher order Zernike terms may lead to a solution with a higher resemblance of the Kirchhoff approximation. The aberrations induced by a plane parallel plate as a function of pupil radius and angle, derived by Mahajan, are

$$\Phi(\rho,\theta) = \frac{(n^2-1)t}{8n^3S^4}(\rho^4 - 4h\rho^3 cos\theta + 4h^2\rho^2 cos^2\theta + 2h^2\rho^2 - 4h^3\rho cos\theta) \quad (2)$$

Where each successive term represents spherical, coma, astigmatism, field curvature, and distortion, respectively [10]. The parameters include the refractive index of the plate, n, plate thickness, t, the object height, h, and the object distance, S. Equation 2 shows that more aberrations besides just spherical aberration may require compensation.

5. CONCLUSIONS AND FUTURE WORK

SMO has improved the process latitude of sub-wavelength features by the smart selection of both source and mask features. Its inadequacy lies in the inability to control the phase, especially when unavoidable aberrations are detrimental to the image. Using a rigorous Maxwell model to include mask topography effects, it has been shown that the FEM shows the characteristic positive BF shift of negative spherical aberration. A simple exhaustive grid search of the z_9 parameter space revealed an improved FEM with a compensating z_9 of +0.06. At this spherical coefficient, the DOF was improved by up to 19%, and the FEM Tilt was reduced by a factor of 10. This shows the capability of the lens pupil domain to compensate for mask topography effects. Since the lens pupil domain would be a significant parameter for SMO, one may want to consider Multiple Domain Optimization (MDO).

Similar optimization with alternate phase shift mask structures, such as dual trench with bias /undercut and Side-wall Chrome Alternating Aperture Mask (SCAAM) will be performed. Certain SMO generated source/mask solutions, such as 1D AttPSM with dipole or 2D contacts with quadrupole, will be evaluated to determine potential for improvement by the lens pupil domain. Experimental validation may be completed using the lens manipulators on state of the art full field scanners [13]. The maximum wavefront deformation capable by the lens manipulators may be limited, thus restricted boundary conditions must be used during optimization.

ACKNOWLEDGEMENTS

This work was supported by the National Science Foundation through a Graduate Research Fellowship to Monica Kempsell Sears and the Semiconductor Research Corporation - Global Research Collaboration through Research Tasks 1459 and 2126. The authors would like to thank KLA-Tencor for the use of PROLITH™ and Robert Socha for valuable discussions.

REFERENCES

[1] Gau, T. S., Liu, R. G., Chen, C. K., Lai, C. M., Liang, F. J., and Hsia C. C., "Customized illumination aperture filter for low k1 photolithography process," Proc. SPIE 4000, 271-282 (2000).

[2] Rosenbluth, A. E., Bukofsky, S. J., Hibbs, M. S., Lai, K., Molless, A. F., Singh, R. N., et al., "Optimum mask and source patterns to print a given shape," Proc. SPIE 4346, 486-502 (2001).

[3] Erdmann, A., and Evanschitzky, P., "Rigorous electromagnetic field mask modeling and related lithographic effects in the low k1 and ultrahigh numerical aperture regime," J. Microlith., Microfab., Microsyst. 6(3), 031002-031016 (2007).

[4] Wong, A. K. K. and Neureuther, A. R., "Mask topography effects in projection printing of phase-shifting masks," Electron Devices, IEEE Transactions on*,* 41(6), 895-902 (1994).

[5] Fukuda, H., Terasawa, T., and Okazaki, S., "Spatial filtering for depth of focus and resolution enhancement in optical lithography," J. Vac. Sci. Technol. B 9(6), 3113-3116 (1991).

[6] Fukuda, H., and Yamanaka, R., "A New Pupil Filter for Annular Illumination in Optical Lithography," Jpn. J. Appl. Phys. 31, 4126-4130 (1992).

[7] von Buenau, R. M., Fukuda, H., and Terasawa, T., "Effects of radially nonsymmetric pupil filters and multiple-pupil exposure," Proc. SPIE 2726, 375-385 (1996).

[8] Gerold, D. J., Petersen, J. S., and Levenson, D., "Multiple pitch transmission and phase analysis of six types of strong phase-shifting masks," Proc. SPIE 4346, 729-743 (2001).

[9] Erdmann, A., "Mask modeling in the low k1 and ultrahigh NA regime: phase and polarization effects (Invited Paper)," Proc. SPIE 5835, 69-81 (2005).

[10] Mahajan, V. N., [Aberration theory made simple], SPIE Optical Engineering Press, Bellingham, 31-34 (1991).

[11] Suzuki, K., and Smith, B., [Microlithography: Science and Technology 2 ed], CRC Press, Boca Raton, 191-194 (2007).

[12] Bencher, C., Dai, H., and Chen, Y., "Gridded design rule scaling: taking the CPU toward the 16nm node," Proc. SPIE 7274, 72740G-10 (2009).

[13] Finders, J., Dusa, M., Nikolsky, P., van Dommelen, Y., Watso, R., Vandeweyer, T., et al. "Litho and patterning challenges for memory and logic applications at the 22-nm node," Proc. SPIE 7640, 76400C-10 (2010).